Article

Ultralow velocity zone and deep mantle flow beneath the Himalayas linked to subducted slab

Jonathan Wolf [1] ✉, Maureen D. Long [1] & Daniel A. Frost[2]

The origins of ultralow velocity zones, small-scale structures with extremely low seismic velocities found near the core–mantle boundary, remain poorly understood. One hypothesis is that they are mobile features that actively participate in mantle convection, but mantle flow adjacent to ultralow velocity zones is poorly understood and difficult to infer. Although deep mantle anisotropy observations can be used to infer mantle flow patterns, ultralow velocity zone structures are often not examined jointly with these observations. Here we present evidence from seismic waves that sample the lowermost mantle beneath the Himalayas for both an ultralow velocity zone and an adjacent region of seismic anisotropy associated with mantle flow. By modelling realistic mineral physics scenarios using global wavefield simulations, we show that the identified seismic anisotropy is consistent with horizontal shearing orientated northeast–southwest. Based on tomographic data of the surrounding mantle structure, we suggest that this southwestward flow is potentially linked to the remnants of the subducted slab impinging on the core–mantle boundary. The detected ultralow velocity zone is located at the southwestern edge of this anisotropic region, and therefore potentially affected by strong mantle deformation in the surrounding area.

Ultralow velocity zones (ULVZs) are thin (tens of kilometres) regions of strongly (up to ~50% in shear velocities V_s)[1] reduced seismic velocities in the lowermost mantle that may be solid or partially molten[2], and whose origins and evolution remain enigmatic[2]. ULVZs often exhibit V_s reductions that are three times those of P waves[1] and density increases of up to 20%[1] compared with the surrounding mantle. It has been suggested that ULVZs are preferentially located at the edges of two extensive antipodal structures with below-average seismic velocities, called large low velocity provinces[1]; however, this potential connection remains debated[3,4]. Previous computational modelling studies have suggested that ULVZs can resist entrainment and mixing into the surrounding mantle under certain conditions, such as a sufficiently large density and buoyancy contrast with the surrounding mantle (for example, due to iron enrichment), and may instead be transported by mantle flow[5,6]. Such global flow models have further shown that mantle flow is capable of displacing dense basal mantle material such as ULVZs[5,6]. Similarly, it has been suggested that if ULVZs originate from heterogeneous accumulations of previously subducted materials, mantle convection may distribute these materials throughout the lowermost mantle, potentially forming ULVZs[4]. Moreover, subducting slabs may generate hot, perhaps molten, anomalies when impinging on the core–mantle boundary (CMB)[7,8]. On the other hand, if ULVZs are solid, they may be composed of iron-rich $(Mg,Fe)O$ of unknown origin[9]. Therefore, the nature and origin of ULVZs may be intimately connected to mantle dynamics around them. Possible flow scenarios in the deep mantle can be tested observationally by investigating seismic anisotropy near ULVZs, potentially giving insights into the interaction between ULVZs and surrounding mantle flow.

[1]Department of Earth and Planetary Sciences, Yale University, New Haven, CT, USA. [2]School of the Earth, Ocean and Environment, University of South Carolina, Columbia, SC, USA. ✉e-mail: jonathan.wolf@yale.edu
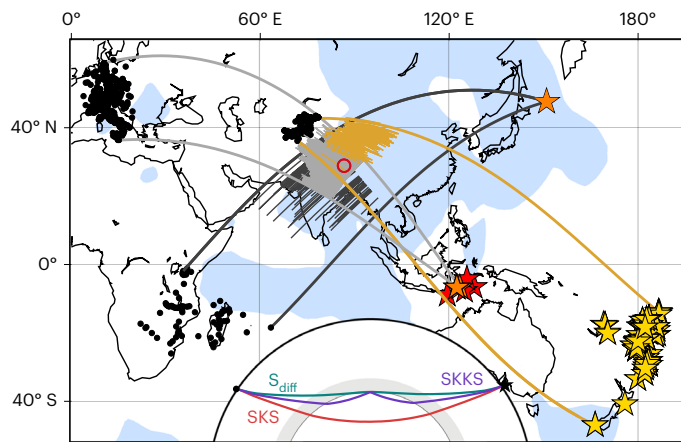
Fig. 1 | Source–receiver configuration used in this study. The three events for which we examined S_{diff} phases across Europe and southern Africa are shown as orange stars and the corresponding stations as black dots. The S_{diff} raypath segments along the CMB are shown as light (European stations) and dark (African stations) grey lines. Long, thick grey lines indicate S_{diff} great circle raypaths at the maximum and minimum S_{diff} azimuth. Events used for SKS splitting measurements, which are compared with S_{diff} splitting measurements for an identical set of stations for each SKS–S_{diff} event pair to constrain potential upper mantle contributions to splitting, are shown as red stars. Events used for the SKS–SKKS differential splitting analysis are shown as yellow stars. The pierce points of SKKS 250 km above the CMB and SKS at the CMB are connected by orange lines. Long, thick orange lines indicate great circle raypaths at the maximum and minimum azimuth for the SKS–SKKS splitting analysis. Blue background colours indicate regions at 2,800 km depth for which seismic velocities are at least 0.4% higher than the global average, according to the GyPSuM[13] tomographic model. The approximate location of a detected ULVZ is shown as a red circle. The inset shows a cross-section of SKS, SKKS and S_{diff} raypaths through Earth (event, black star; station, black circle).

Owing to favourable seismic raypath coverage (Fig. 1), the lowermost mantle beneath the Himalayas is an ideal place to investigate relationships between mantle flow and ULVZs. The region is probably dominated by remnant slabs[10,11], leading to generally higher than average seismic velocities[12,13] because their temperature is colder than the surrounding mantle. Today, remnants of the Central China slab have probably reached the CMB in this region[11]. Therefore, deep mantle flow may plausibly be slab-driven, similar to other locations in the deep mantle with comparatively high seismic velocities[14,15]. Here we investigate flow and deformation directions at the base of the mantle by measuring seismic anisotropy (directionally dependent seismic wavespeeds), a relatively direct indicator of deformation[16]. The presence of seismic anisotropy and ULVZs is usually investigated separately[1,17], despite their potential connections to fundamental aspects of deep Earth dynamics. Here we systematically study both anisotropy and ULVZ structure in the deep mantle beneath the Himalayas, building on previous evidence for ULVZ structure nearby[3]. Recent methodological progress enables us to jointly analyse S_{diff} phases, S waves that are diffracted along the CMB (Fig. 1 inset), for both lowermost mantle anisotropy and ULVZ structure[18–20]. We supplement our anisotropy analysis with SKS and SKKS (Fig. 1) data. We connect our anisotropy observations with the presence of an ULVZ beneath the Himalayas. We suggest that the ULVZ is potentially affected by mantle flow adjacent to it, perhaps being displaced by active convection[6,21]; furthermore, the ULVZ present in our study region may originate from subducted material[4], or be generated by slab material impinging on the CMB[7,8].

Deep mantle anisotropy analysis

Following the strategy laid out in ref. 22, we investigate S_{diff} waveforms from three high-quality events, which we call events 1–3 (Supplementary Table 1). We analyse waveforms from these earthquakes measured

at seismic stations across Europe and southern Africa (Fig. 1), sampling our study region across two distinct directions. Events 1 and 2 have favourable initial polarizations (Extended Data Fig. 1 and Supplementary Fig. 1) and can therefore be used for the analysis of seismic anisotropy, while event 3 is substantially SV-polarized (Supplementary Fig. 2) and is only used for ULVZ analysis. For events 1 and 2, we stack waveforms for epicentral distances 105–115° as a function of azimuth in 1.5° bins (Fig. 2b and Extended Data Fig. 1). Global wavefield simulations using the isotropic GyPSuM[13] Earth model show that the initial source polarization for these events is such that in the absence of seismic anisotropy, almost no radial component energy is expected to arrive for raypaths at azimuths >315° (Extended Data Fig. 1a). However, clear radial energy can in fact be observed for both events for azimuths >321° (Fig. 2b and Extended Data Fig. 1b), indicating shear-wave splitting. To distinguish whether splitting occurs in Earth's upper layers or the lowermost mantle, we compare S_{diff} waveforms from events 1 and 2 with SKS waveforms from five events that occurred in a similar location (Fig. 1 and Supplementary Table 2) and show strong SKS energy due to their favourable initial polarization. SKS is typically mainly affected by anisotropy in the upper mantle beneath the station[23]; furthermore, by stacking we are essentially averaging the upper mantle splitting contribution[24] over a complex and heterogeneous area[25]. The absence of notable transverse component energy for the SKS events for northerly raypaths (azimuths ~321°) indicates that, at this azimuth range, S_{diff} is also largely unaffected by anisotropy beneath the receiver. Therefore, the large radial component amplitudes in the S_{diff} azimuth stacks for events 1 and 2 indicate a likely contribution of lowermost mantle anisotropy to S_{diff} splitting (Extended Data Fig. 1). In this comparison we only use stations that recorded both phases (SKS and S_{diff}) in our analysis.

We measure splitting parameters from the 1.5°-bin azimuth stacks of SKS and S_{diff} (Supplementary Figs. 3 and 4). Specifically, we estimate splitting intensity[26] (SI), fast polarization direction (ϕ or ϕ'')[22] and time delay (δt). These splitting parameters estimated from the stacked data can be interpreted as a spatially averaged anisotropic contribution[24]. For those azimuths for which SKS splitting is effectively null ($SI < 0.3$) and S_{diff} splitting is not, we determine (ϕ'', δt) for S_{diff} and attribute this splitting to lowermost mantle anisotropy (Supplementary Figs. 3 and 4). We perform such an analysis for all five SKS events (Supplementary Table 2), all of which show null or nearly null SKS splitting for azimuths around 321°, for which S_{diff} waveforms of events 1 and 2 are clearly split. We then combine the splitting results for events 1 and 2 by calculating averages, weighted by the square of the 95% confidence interval for each azimuth bin, which leads to tighter confidence intervals than focusing on individual earthquakes. We obtain robust splitting measurements for three azimuth bins (Fig. 2b,c and Supplementary Figs. 3 and 4); each yields nearly identical fast polarization directions ($\phi'' \approx 45°$) for both S_{diff} events. Because the fast polarization direction is the same for all three azimuth bins for events 1 and 2, we assume that the sampled anisotropic region and deformation geometry is also the same; however, the strength of the apparent splitting differs for different azimuth bins. We show the geographic distribution of S_{diff} raypaths along the CMB in Fig. 2c, marking those waveforms that are clearly influenced by lowermost mantle anisotropy.

Complementary to our S_{diff} measurements, we additionally analyse differential splitting of SKS–SKKS phase pairs (Extended Data Fig. 2 and Supplementary Table 3). Because SKS and SKKS sample the upper mantle in a similar way, but sample the lowermost mantle differently, strongly discrepant SKS–SKKS splitting indicates a likely contribution to one or both phases from D″ anisotropy[27]. We designate as discrepant pairs of phases for which $\delta SI > 0.4$ (following previous work[27,28]). We analyse differential SKS–SKKS splitting for stations in central Asia (Fig. 1), for which SKS and SKKS raypaths sample the lowermost mantle in a similar location to our S_{diff} measurements. We observe that SKS–SKKS pairs for which one of the phases samples the lowermost mantle
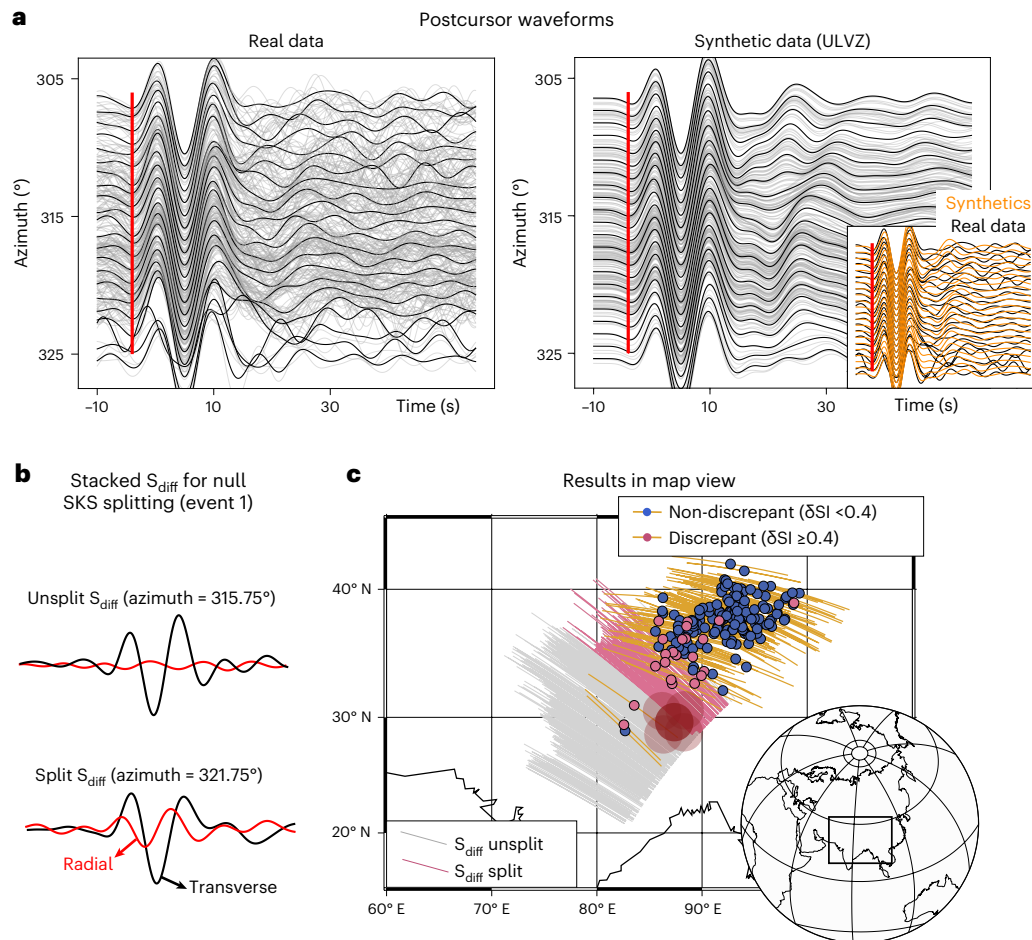
Fig. 2 | Summary of ULVZ and anisotropy results. a, Left: transverse velocity S_{diff} waveforms from event 1 as a function of azimuth, bandpass-filtered to retain periods between 7 and 25 seconds and aligned with respect to the maximum S_{diff} amplitude. Waveforms are linearly stacked in 1° bins. Individual waveforms are shown as grey lines and azimuthal stacks as black lines. Postcursors, characteristic for the presence of ULVZ structure along the raypath, are visible in the ~30 seconds after the S_{diff} arrival; their timing varies as a function of azimuth. The approximate S_{diff} arrival is shown by a vertical red line. Right: similar to left panel but for GyPSuM[13] synthetics, incorporating the cylindrical ULVZ with a velocity reduction of 36% and a radius of 1.5°, centred at 87.0° E, 29.5° N. The inset shows azimuthal seismogram stacks for synthetic (yellow) and real (black) data. **b**, Stacked radial (black line) and transverse (red line) S_{diff} velocity seismograms for event 1, bandpass-filtered to retain periods between 8 and 25 seconds. Linear stacks are calculated for 1.5°-wide azimuth bins, centred at azimuths 315.75°

and 321.75°. Stacks for all bins are shown in Supplementary Fig. 1. For both azimuth bins, SKS splitting is (almost) null (Supplementary Fig. 3). Therefore, the top (unsplit) S_{diff} waveforms indicate the absence, and the bottom (split) S_{diff} waveforms the presence, of splitting due to lowermost mantle anisotropy. **c**, ULVZ and anisotropy results in map view. SKS–SKKS differential splitting analysis: orange lines connect the pierce point of SKKS 250 km above the CMB and the pierce point of SKS at the CMB. In the middle of the orange lines, coloured circles indicate non-discrepant (blue) or discrepant (pink) SKS–SKKS splitting (see legend). S_{diff} splitting: the great circle raypath length of S_{diff} along the CMB is represented by grey (no lowermost mantle splitting) or pink (lowermost mantle splitting) lines (see legend). Raypaths of event 3 are not shown because this event was not used in the splitting analysis. ULVZ structure: the best-fitting cylindrical ULVZ is shown as a dark red circle, with light red circles indicating the location uncertainty.

close to where we have inferred the presence of deep mantle anisotropy from S_{diff} tend to exhibit discrepant splitting, while splitting tends to be non-discrepant further away from our identified anisotropic region (Fig. 2b). Our observation of discrepant SKS–SKKS splitting is an additional piece of evidence that S_{diff} probably samples lowermost mantle anisotropy at the CMB, and not (only) on the other portions of the raypath.

ULVZ location and properties

We infer the presence of a ULVZ in our study region from the postcursors[18,29] arriving after the S_{diff} phase on transverse component record sections of events 1–3 (Fig. 2a, and Supplementary Figs. 5 and 6). A beamforming approach[30] reveals that, as expected for wave refraction due to ULVZ structure[18], these postcursors come in from a slightly more northerly backazimuth than the main S_{diff} arrival for stations in Italy (Extended Data Fig. 3). We conduct fully three-dimensional (3D) global wavefield simulations to model the location and properties of

the ULVZ simultaneously using AxiSEM3D[31,32]. We simulate a cylindrical ULVZ region with a thickness of 20 km and vary its location, lateral extent and velocity reduction through forward modelling, with the goal of matching the timing of the observed postcursors for all three events. The best-fitting combination of ULVZ properties involves a shear-wave velocity reduction between 32% and 40% (compared with the Preliminary reference Earth model (PREM)[33]) for a radius of 1.5° (or a higher velocity reduction for a smaller ULVZ), and a location centred approximately at 87.0° E, 29.5° N (Supplementary Figs. 7–13). The best-fitting ULVZ model is selected to match well the delay times of the S_{diff} postcursors relative to the main S_{diff} arrival seen in the real data (Fig. 2a). There are substantial tradeoffs between size and velocity reduction (Supplementary Figs. 7–11). Generally, the smaller the size of the ULVZ, the lower the best-fitting velocities needed to produce similar postcursors[18,20]. These tradeoffs, however, do not change the best-fitting centre location of the ULVZ[18,20], which is the most important aspect for the interpretation of our results. Importantly, waveform
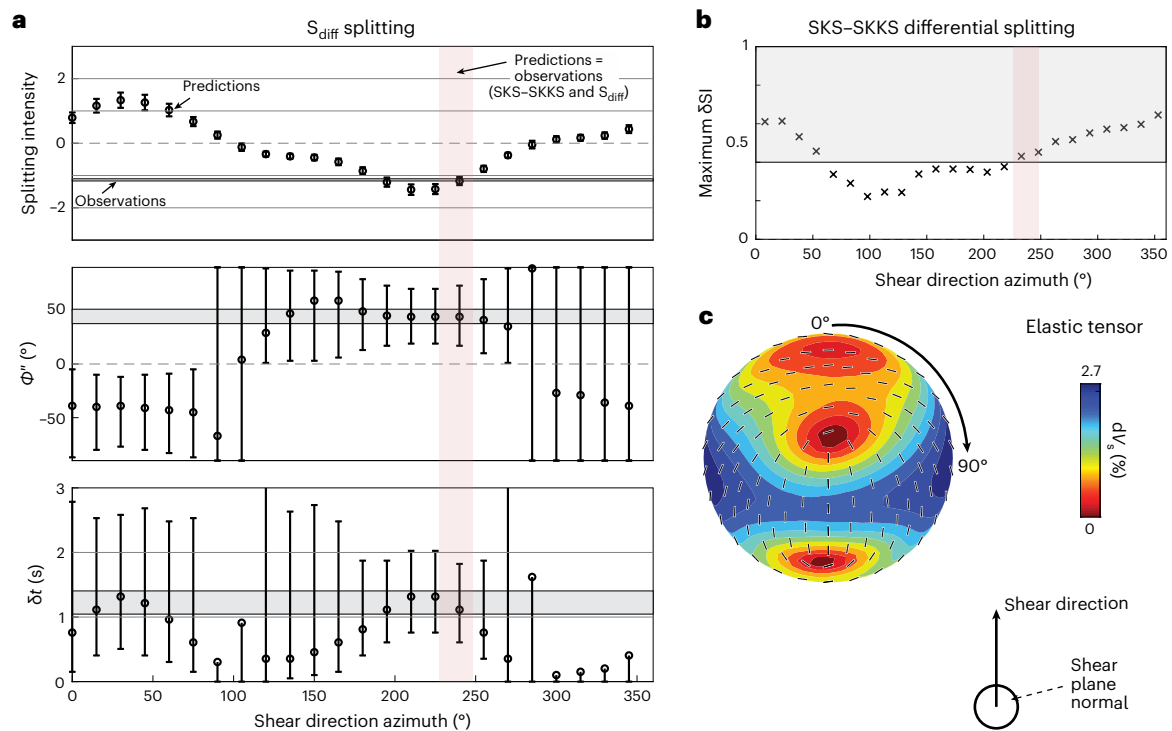
Fig. 3 | Comparison between observations and model results for a Ppv elastic tensor with a dominant slip system of [100](010). a, Top panel: symbols show splitting parameters for stacked synthetic seismograms for event 2, generated for a model with a 110-km-thick Ppv layer at the base of the mantle, plotted as a function of shear direction azimuth, in degrees from north. Error bars represent 95% confidence intervals (standard errors around the best-fitting measurement) determined with SplitRacer[41] for the synthetic measurements determined using 30 randomly chosen time windows (Methods). Grey shaded areas indicate the 95% confidence intervals (standard errors) of the five events conducted for all stations that recorded event 2, weighted by the squared size of the individual splitting measurements made using 30 random time windows. Light red shading indicates the range of shear direction azimuths that are consistent with our observations. Middle and bottom panels: like the top panel but for ϕ'' and δt. **b**, Maximum splitting intensity difference (δSI) between SKS and SKKS as a function of shear direction azimuth; this is the maximum SKS–SKKS discrepancy when either SKS or SKKS, or both, sample the lowermost mantle anisotropy. Light red shading again indicates the range of shear direction azimuths that are consistent with our observations, and grey shading indicates splitting intensity differences >0.4 (discrepant splitting). **c**, Upper hemisphere representation of the Ppv elastic tensor used in the simulation. Black sticks represent fast S polarization directions and background colours the amplitude of V_s anisotropy (in %) at each direction. The shear plane is oriented horizontally and the tensor is rotated in the horizontal plane (clockwise from north) to test different candidate shear directions.

effects from ULVZ structure do not mimic splitting due to seismic anisotropy[22] (Supplementary Fig. 14). Owing to the existence of crossing raypaths, the best-fitting location of the ULVZ can be identified relatively precisely (Fig. 2b). We show postcursor waveforms for the real-data event 1 and the synthetic seismograms for our best-fitting cylindrical ULVZ model in Fig. 2a. The postcursor delay times for events 1 and 2 (Supplementary Figs. 5, 7 and 8) are very similar as their hypocentres are very close to each other, while event 3 gives independent constraints from a crossing direction (Fig. 1).

Shear direction modelling and geodynamic interpretations

In order to constrain the likely flow and deformation geometry at the base of the mantle, we carry out a series of forward modelling experiments to simulate global wave propagation through models that include lowermost mantle anisotropy, attempting to reproduce the measured S_{diff} and SKS–SKKS splitting. The lowermost mantle beneath the Himalayas is probably dominated by slab remnants[10], implying lower than average temperatures and a relatively shallow bridgmanite–postperovskite transition[34]. It is therefore likely that lattice-preferred orientation of postperovskite (Ppv)[35,36] is the dominant mechanism for anisotropy in this region, and not shape-preferred orientation due to partial melt, which is more likely in the hotter regions of the mantle. We also explored models for two other candidate minerals that may develop lattice-preferred orientation in the lowermost mantle, bridgmanite and ferropericlase, but these are unable to simultaneously

explain our S_{diff} and SKS–SKKS splitting observations (Supplementary Figs 15–18).

We model anisotropic Ppv using a library of plausible lowermost mantle elastic tensors[37] in our wavefield simulations, assuming a horizontal shear direction and 100% strain. (Note that a different degree of strain would mainly affect the strength of splitting, but not the geometry of the anisotropy[37] (Supplementary Fig. 19), which is the most important factor in our interpretation.) We consider a variety of potential shear directions by rotating the candidate elastic tensors in increments of 15° in the horizontal plane. The tensors we use are based on single-crystal elasticity predicted by two different studies[35,36] and were modelled in ref. 37 using three different candidate dominant slip systems: [100](010), [100](001) and {011}<0–11> + (010)<100> slip. We conduct these simulations with the goal of matching S_{diff} splitting for events 1 and 2. We adjust the layer thickness to match the observed splitting strength, and assume homogeneous anisotropy along the whole S_{diff} raypath through the lowermost mantle. We also examine SKS–SKKS discrepancies for the same set of simulations; this is straightforward, given that SKS–SKKS splitting intensity discrepancies are independent of the focal mechanism and that the synthetics are noise-free, thus also reliably recording the small SKS and SKKS amplitudes. In this comparison, we correct for the slight difference in backazimuth of SK(K)S raypaths compared to S_{diff} (Fig. 1).

We investigate the range of shear direction orientations for which the S_{diff} splitting parameters from our synthetic simulations agree with our real-data observations (Fig. 3a). As an additional constraint,
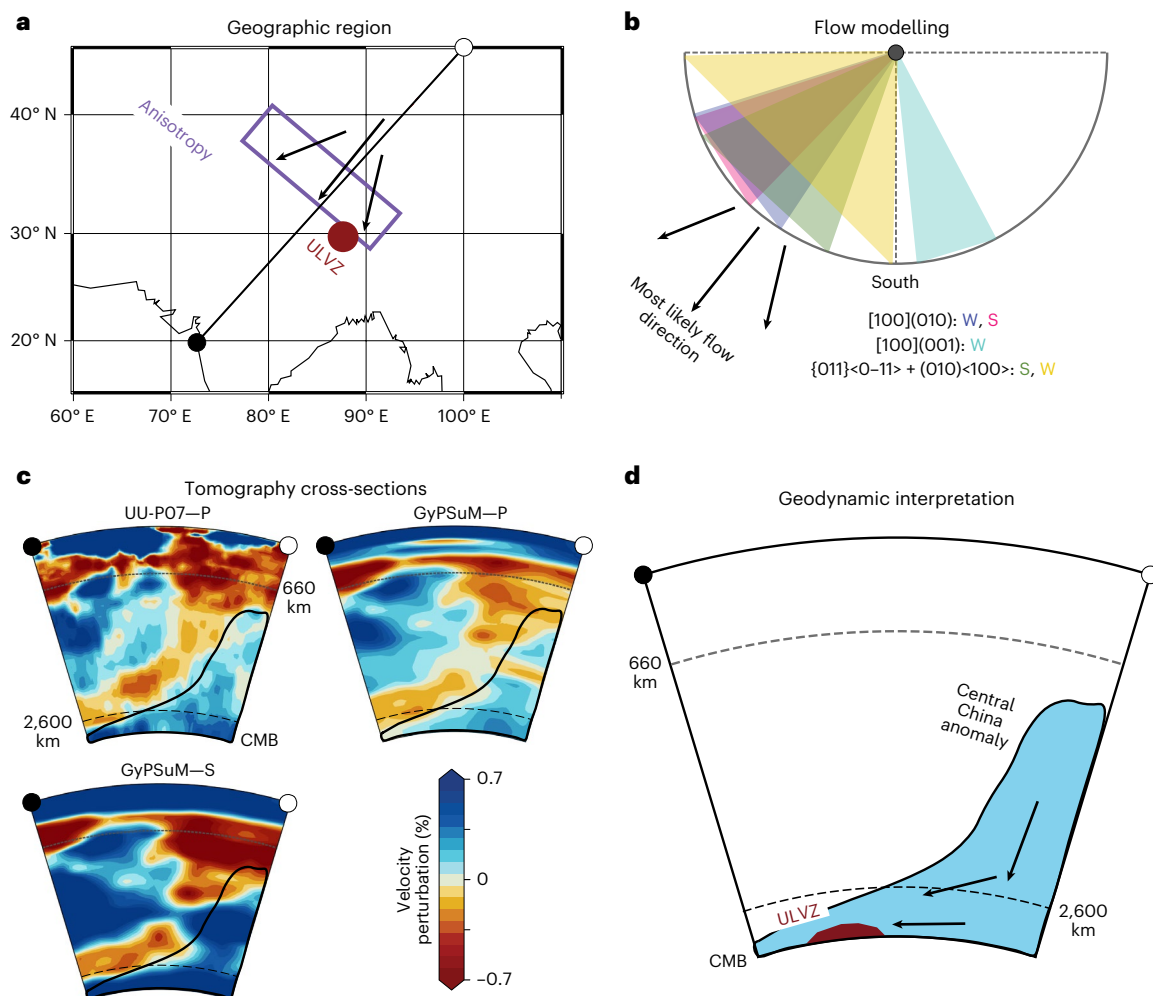
Fig. 4 | Summary of results and interpretations. a, We identify a large anisotropic region (violet box), consistent with southwestwards mantle flow (arrows), next to an ULVZ (red circle), approximately located beneath the Himalayas. **b**, Modelling using four out of six Ppv elastic tensors tested suggests flow in a southwest (or, equivalently, northeast) direction, with one elastic tensor suggesting flow in a south–southeast (or, equivalently, north–northwest) direction. The sixth Ppv elastic tensor is generally incompatible with our splitting observations (see Supplementary Fig. 15). Triangles show the range of shear directions compatible with the splitting data for each candidate elastic tensor. We only show southeast and southwest quadrants, but there is a 180° ambiguity in the potential shear direction. The legend shows the slip systems considered, and whether the single-crystal elasticity used to construct the tensors relied on predictions from Stackhouse et al.[35] (S) or Wentzcovitch et al.[36] (W), in the corresponding colour. **c**, Slices from the UU-P07[12] and GyPSuM[13] tomography models through our study region, with the start and end points (black and white circle, respectively) shown in **a**. The deep mantle high-velocity feature shown in **d** is outlined. Slow anomalies, whose origins are poorly understood, dominate the mid-mantle. **d**, Interpretation of the fast velocity anomaly shown in **c** in the lowermost mantle as corresponding to the Central China slab, following ref. 11. The inferred mantle flow from our study is shown by black arrows and the ULVZ (vertically and laterally exaggerated for clarity) we identify is shown in dark red.

we require candidate models to predict discrepant SKS–SKKS splitting, matching the observations for the anisotropic region (Fig. 3b). Figure 3 shows an example for an elastic tensor with dominant [100](010) slip, for which shear orientation azimuths between 225° and 240° fit our observations. The anisotropic modelling results for the other Ppv elastic tensors are shown in Supplementary Figs. 20–24. Overall, for four out of six Ppv elastic tensors, southwest (or, equivalently, northeast) directions are compatible with our splitting observations. One elastic tensor (for [100](001) slip) indicates a different flow direction (south–southeast or north–northwest; Fig. 4b), and the sixth elastic tensor is incompatible with our splitting observations because it is unable to reproduce the magnitude of the real splitting data, even when assuming an unrealistically thick (400 km) anisotropic layer at the base of the mantle (Supplementary Fig. 21). Taken together, our anisotropic modelling results generally indicate either northeast or southwest-directed flow in the lowermost mantle beneath the Himalayas (Fig. 4b). However, flow in south–southeast or north–northwest

direction cannot be fully excluded, as one Ppv texture model predicts this (Supplementary Fig. 22).

Tomographic imaging (Fig. 4c) shows that our study region is dominated by slow anomalies in the mid-mantle whose origins are poorly understood, and by fast anomalies to the northwest and at the base of the mantle, which probably correspond to remnant slabs[10,11]. We suggest that deformation due to slab-driven flow, which produces lattice-preferred orientation and seismic anisotropy, is a plausible explanation for our observations at the base of the mantle. A recent study[11] inferred that the high-velocity anomaly visible in the lowermost mantle in our study region (Fig. 4c,d), which has a typical shape for a subducted remnant slab[10], corresponds to the subducted Central China anomaly, which extends in a southwest direction along the CMB. Given its present-day extent to the southwest, the Central China slab has probably moved laterally along the CMB[11], thereby driving flow to the southwest, in agreement with our anisotropy measurements. Owing to its location hundreds of kilometres above the CMB, the mid-mantle low

velocity feature probably has no direct effect on our seismic anisotropy measurements, and is therefore not critical for our interpretation.

We can compare this inferred flow with predictions from previous global models of flow and anisotropy. Two studies[38,39] suggest weak flow in a northeast direction in our study region, while the model of another[40] predicts strong southwestward flow. The first two studies based their flow direction calculations mainly on density variations derived from global tomography models, whereas ref. 40 used palaeo-geographic plate reconstructions to model flow. The good agreement between this model and the likeliest flow directions we infer suggest that in this region, flow at the base of the mantle may have a connection to the history of subduction at the surface.

The detected ULVZ is located at the southwestern edge of the inferred anisotropic region (Fig. 4), which is probably linked to south-westwards flow induced by the Central China slab (Fig. 4). While we cannot uniquely constrain the history of deformation and its influence on the ULVZ from the present-day characteristics, the current configuration suggests some plausible geodynamic scenarios. One possibility is that the ULVZ formed at its present-day location and is stationary, and the strong mantle deformation just adjacent to it is coincidental. However, it is also possible that the ULVZ is actively pushed to the southwest by slab remnants, which would explain its location at the edge of the anisotropic region (Fig. 4). In this case, it would be participating in mantle flow, as previously suggested by geodynamic simulations[6,21]. Furthermore, the coincidence of likely slab remnants in the deep mantle in proximity to the ULVZ raises the possibility that the ULVZ itself is composed of subducted slab material[4] from the Central China slab, or has been formed through slab impingement on the CMB[7,8].

Online content

Any methods, additional references, Nature Portfolio reporting summaries, source data, extended data, supplementary information, acknowledgements, peer review information; details of author contributions and competing interests; and statements of data and code availability are available at https://doi.org/10.1038/s41561-024-01386-5.

References

1. Yu, S. & Garnero, E. J. Ultralow velocity zone locations: a global assessment. *Geochem. Geophys. Geosyst.* **19**, 396–414 (2018).
2. McNamara, A. K. A review of large low shear velocity provinces and ultra low velocity zones. *Tectonophysics* **760**, 199–220 (2019).
3. Thorne, M. S. et al. The most parsimonious ultralow-velocity zone distribution from highly anomalous SPdKS waveforms. *Geochem. Geophy. Geosyst.* **22**, e2020GC009467 (2021).
4. Hansen, S. E., Garnero, E. J., Li, M., Shim, S.-H. & Rost, S. Globally distributed subducted materials along the Earth's core–mantle boundary: implications for ultralow velocity zones. *Sci. Adv.* **9**, eadd4838 (2023).
5. McNamara, A. & Zhong, S. Thermochemical structures beneath Africa and the Pacific Ocean. *Nature* **437**, 1136–1139 (2005).
6. McNamara, A. K., Garnero, E. J. & Rost, S. Tracking deep mantle reservoirs with ultra-low velocity zones. *Earth Planet. Sci. Lett.* **299**, 1–9 (2010).
7. Tackley, P. J. Living dead slabs in 3-D: the dynamics of compositionally-stratified slabs entering a "slab graveyard" above the core–mantle boundary. *Phys. Earth Planet. Inter.* **188**, 150–162 (2011).
8. Li, M. The formation of hot thermal anomalies in cold subduction-influenced regions of Earth's lowermost mantle. *J. Geophys. Res. Solid Earth* **125**, e2019JB019312 (2020).
9. Lai, V. H. et al. Strong ULVZ and slab interaction at the northeastern edge of the Pacific LLSVP favors plume generation. *Geochem. Geophys. Geosyst.* **23**, e2021GC010020 (2022).
10. van der Meer, D. G., van Hinsbergen, D. J. & Spakman, W. Atlas of the underworld: slab remnants in the mantle, their sinking history, and a new outlook on lower mantle viscosity. *Tectonophysics* **723**, 309–448 (2018).
11. Qayyum, A. et al. Subduction and slab detachment under moving trenches during ongoing India–Asia convergence. *Geochem. Geophys. Geosyst.* **23**, e2022GC010336 (2022).
12. Amaru, M. *Global Travel Time Tomography With 3-D Reference Models*. PhD dissertation, Utrecht Univ. (2007).
13. Simmons, N. A., Forte, A. M., Boschi, L. & Grand, S. P. GyPSuM: A joint tomographic model of mantle density and seismic wave speeds. *J. Geophys. Res. Solid Earth* **115**, B12310 (2010).
14. Asplet, J., Wookey, J. & Kendall, M. A potential post-perovskite province in D″ beneath the eastern Pacific: evidence from new analysis of discrepant SKS–SKKS shear-wave splitting. *Geophys. J. Int.* **221**, 2075–2090 (2020).
15. Wolf, J. & Long, M. D. Slab-driven flow at the base of the mantle beneath the northeastern Pacific Ocean. *Earth Planet. Sci. Lett.* **594**, 117758 (2022).
16. Long, M. D. & Becker, T. Mantle dynamics and seismic anisotropy. *Earth Planet. Sci. Lett.* **297**, 341–354 (2010).
17. Wolf, J., Long, M. D., Li, M. & Garnero, E. Global compilation of deep mantle anisotropy observations and possible correlation with low velocity provinces. *Geochem. Geophys. Geosyst.* **24**, e2023GC011070 (2023).
18. Cottaar, S. & Romanowicz, B. An unusually large ULVZ at the base of the mantle near Hawaii. *Earth Planet. Sci. Lett.* **355–356**, 213–222 (2012).
19. Cottaar, S. & Romanowicz, B. Observations of changing anisotropy across the southern margin of the African LLSVP. *Geophys. J. Int.* **195**, 1184–1195 (2013).
20. Wolf, J. & Long, M. D. Lowermost mantle structure beneath the central Pacific Ocean: ultralow velocity zones and seismic aniso-tropy. *Geochem. Geophys. Geosyst.* **24**, e2022GC010853 (2023).
21. Li, M., McNamara, A., Garnero, E. & Yu, S. Compositionally-distinct ultra-low velocity zones on Earth's core–mantle boundary. *Nat. Commun.* **8**, 177 (2017).
22. Wolf, J., Long, M. D., Creasy, N. & Garnero, E. On the measurement of S_{diff} splitting caused by lowermost mantle anisotropy. *Geophys. J. Int.* **233**, 900–921 (2023).
23. Long, M. D. & Silver, P. G. Shear wave splitting and mantle anisotropy: measurements, interpretations, and new directions. *Surv. Geophys.* **30**, 407–461 (2009).
24. Wolf, J. et al. Observations of mantle seismic anisotropy using array techniques: shear-wave splitting of beamformed SmKS phases. *J. Geophys. Res. Solid Earth* **128**, e2022JB025556 (2023).
25. Hein, G., Kolínský, P., Bianchi, I., Bokelmann, G. & Group, A. W. Shear wave splitting in the Alpine region. *Geophys. J. Int.* **227**, 1996–2015 (2021).
26. Chevrot, S. Multichannel analysis of shear wave splitting. *J. Geophys. Res. Solid Earth* **105**, 21579–21590 (2000).
27. Tesoniero, A., Leng, K., Long, M. D. & Nissen-Meyer, T. Full wave sensitivity of SK(K)S phases to arbitrary anisotropy in the upper and lower mantle. *Geophys. J. Int.* **222**, 412–435 (2020).
28. Wolf, J., Long, M. D., Leng, K. & Nissen-Meyer, T. Constraining deep mantle anisotropy with shear wave splitting measurements: challenges and new measurement strategies. *Geophys. J. Int.* **230**, 507–527 (2022).
29. Li, Z., Leng, K., Jenkins, J. & Cottaar, S. Kilometer-scale structure on the core–mantle boundary near Hawaii. *Nat. Commun.* **13**, 2787 (2022).
30. Frost, D. A., Romanowicz, B. & Roecker, S. Upper mantle slab under Alaska: contribution to anomalous core-phase observations on south-Sandwich to Alaska paths. *Phys. Earth Planet. Inter.* **299**, 106427 (2020).

31. Leng, K., Nissen-Meyer, T. & van Driel, M. Efficient global wave propagation adapted to 3-D structural complexity: a pseudo-spectral/spectral-element approach. *Geophys. J. Int.* **207**, 1700–1721 (2016).

32. Leng, K., Nissen-Meyer, T., van Driel, M., Hosseini, K. & Al-Attar, D. AxiSEM3D: broad-band seismic wavefields in 3-D global Earth models with undulating discontinuities. *Geophys. J. Int.* **217**, 2125–2146 (2019).

33. Dziewonski, A. M. & Anderson, D. L. Preliminary reference Earth model. *Phys. Earth Planet. Inter.* **25**, 297–356 (1981).

34. Murakami, M., Hirose, K., Kawamura, K., Sata, N. & Ohishi, Y. Post-perovskite phase transition in $MgSiO_3$. *Science* **304**, 855–858 (2004).

35. Stackhouse, S., Brodholt, J. P., Wookey, J., Kendall, J.-M. & Price, G. D. The effect of temperature on the seismic anisotropy of the perovskite and post-perovskite polymorphs of $MgSiO_3$. *Earth Planet. Sci. Lett.* **230**, 1–10 (2005).

36. Wentzcovitch, R. M., Tsuchiya, T. & Tsuchiya, J. $MgSiO_3$ postperovskite at D″ conditions. *Proc. Natl Acad. Sci. USA* **103**, 543–546 (2006).

37. Creasy, N., Miyagi, L. & Long, M. D. A library of elastic tensors for lowermost mantle seismic anisotropy studies and comparison with seismic observations. *Geochem. Geophys. Geosyst.* **21**, e2019GC008883 (2020).

38. Walker, A. M., Forte, A. M., Wookey, J., Nowacki, A. & Kendall, J.-M. Elastic anisotropy of D″ predicted from global models of mantle flow. *Geochem. Geophys. Geosyst.* **12**, Q10006 (2011).

39. Forte, A. Constraints on seismic models from other disciplines - implications for mantle dynamics and composition. *Treatise Geophys.* **1**, 805–858 (2015).

40. Flament, N. Present-day dynamic topography and lower-mantle structure from palaeogeographically constrained mantle flow models. *Geophys. J. Int.* **216**, 2158–2182 (2018).

41. Reiss, M. & Rümpker, G. SplitRacer: MATLAB code and GUI for semiautomated analysis and interpretation of teleseismic shear-wave splitting. *Seismol. Res. Lett.* **88**, 392–409 (2017).

Methods

Shear-wave splitting measurements

An initially linearly polarized shear wave travelling through an anisotropic medium splits into two quasi-shear waves, travelling at different speeds[42]. The splitting parameters can be expressed through the polarization direction of the fast wave, measured either with respect to the north (ϕ) or the backazimuthal direction (ϕ')[43], and the relative time shift (δt) between slow and fast waves. These two quantities (ϕ', δt) are related to the splitting intensity[26], which can be expressed as:

$$\text{SI} = -2 \frac{C_{90}(t)C_0'(t)}{|C_0'(t)|^2} \approx \delta t \sin(-2\phi'), \qquad (1)$$

with $C_{90}(t)$ denoting the horizontal seismogram component oriented 90° away from to the incoming wave's initial polarization and C_0 the time derivative of the component corresponding to the direction of initial polarization. Thus, for S(K)KS waves (Fig. 1a) C_0 corresponds to the radial component; for S_{diff} waves with a favourable initial polarization (Fig. 1a), C_0 corresponds to the transverse component[22].

We measure shear-wave splitting parameters with the MATLAB-based graphical user interface SplitRacer[41]. SplitRacer calculates splitting parameters using the transverse energy minimization technique[41] using a corrected error formulation[44]. SplitRacer automatically picks an ensemble of random time windows to ensure that measurements do not depend on a particular measurement window selection. In our analysis we always measure splitting on waveforms that have been bandpass-filtered to retain energy at periods between 8 and 25 seconds.

Because SKS and SKKS raypaths have a large spatial separation in the lowermost mantle but are nearly coincident in the upper mantle (Fig. 1a), large differences in SKS–SKKS splitting intensities (>0.4) for the same event–station pair can be attributed to lowermost mantle anisotropy[27]. For our SKS–SKKS analysis, which closely follows previous work[45], we focus on data for which both phases exhibit signal-to-noise ratios larger than 3, since it has been shown that noise can have non-negligible effects on SK(K)S splitting intensities[24].

To measure S_{diff} splitting, we follow the strategy laid out in previous work[22]. We ensure that the focal mechanism is such that S_{diff} would be almost purely SH-polarized in an isotropic Earth (Supplementary Figs. 1 and 2). We analyse only deep events (focal depths >500 km) to exclude the possibility of strong (SI >1.0) source-side anisotropy. We avoid the need for explicit receiver-side anisotropy corrections, because SKS splitting averaged over the heterogeneous upper mantle[25] beneath Europe is null (Supplementary Figs. 3 and 4). Furthermore, we can isolate the likely location of seismic anisotropy along the S_{diff} raypath to be in the lower mantle by using complementary measurements of differential SKS–SKKS splitting. As in previous work[22], we use a version of SplitRacer modified to measure S_{diff} and call the resulting fast polarization direction ϕ'' (= 90° − ϕ').

Global wavefield simulations

We carry out fully 3D global simulations of the seismic wavefield using AxiSEM3D[31,32]. All our simulations include Earth's ellipticity and PREM attenuation[33]. The focal mechanisms for the earthquakes are taken from the Global Centroid Moment Tensor Catalog[46]. To conduct global wavefield simulations for anisotropic input models, we calculate synthetic seismograms down to periods of ~6 s, following our previous work[47]. The background model for most of our anisotropy simulations is isotropic PREM. We systematically add anisotropic regions to our models using elastic tensors based on textured Ppv, bridgmanite and ferropericlase from the elastic tensor library of ref. 37, for simple shear deformation with 100% strain.

For our ULVZ simulations, we always use a PREM[33] background mesh, resolving minimum periods of 5 seconds. In most simulations, we replace the PREM mantle with the 3D tomographic model GyPSuM[13],

in order to test the effects of 3D velocity heterogeneity on the S_{diff} wavefield. Our general approach to model setup and parameterization is similar to our previous work that investigated ULVZ structure beneath the central Pacific Ocean[20]. We ensure that AxiSEM3D can accurately resolve the incorporated ULVZ structure by benchmarking our simulations against higher accuracy runs (with a larger number of terms use in the Fourier expansion[32]) and make full use of the incorporated wavefield learning[32] tool in AxiSEM3D for similar simulations. We discuss the full range of model runs in our ULVZ simulations in the Supplementary Information. The Generic Mapping Tools[48], SubMachine[49], ObsPy[50] and MSAT[51] were used in this research.

References

42. Silver, P. G. & Chan, W. W. Shear wave splitting and subcontinental mantle deformation. *J. Geophys. Res. Solid Earth* **96**, 16429–16454 (1991).
43. Nowacki, A., Wookey, J. & Kendall, J.-M. Deformation of the lowermost mantle from seismic anisotropy. *Nature* **467**, 1091–1094 (2010).
44. Walsh, E., Arnold, R. & Savage, M. K. Silver and Chan revisited. *J. Geophys. Res. Solid Earth* **118**, 5500–5515 (2013).
45. Reiss, M., Long, M. D. & Creasy, N. Lowermost mantle anisotropy beneath Africa from differential SKS–SKKS shear-wave splitting. *J. Geophys. Res. Solid Earth* **124**, 8540–8564 (2019).
46. Ekström, G., Nettles, M. & Dziewonski, A. The global CMT project 2004–2010: centroid-moment tensors for 13,017 earthquakes. *Phys. Earth Planet. Inter.* **200–201**, 1–9 (2012).
47. Wolf, J., Long, M. D., Leng, K. & Nissen-Meyer, T. Sensitivity of SK(K)S and ScS phases to heterogeneous anisotropy in the lowermost mantle from global wavefield simulations. *Geophys. J. Int.* **228**, 366–386 (2022).
48. Wessel, P. & Smith, W. H. F. New, improved version of Generic Mapping Tools released. *Eos* **79**, 579–579 (1998).
49. Hosseini, K. et al. SubMachine: web-based tools for exploring seismic tomography and other models of Earth's deep interior. *Geochem. Geophys. Geosyst.* **19**, 1464–1483 (2018).
50. Beyreuther, M. et al. ObsPy: a Python toolbox for seismology. *Seismol. Res. Lett.* **81**, 530–533 (2010).
51. Walker, A. & Wookey, J. MSAT—a new toolkit for the analysis of elastic and seismic anisotropy. *Comput. Geosci.* **49**, 81–90 (2012).

Author contributions

Conceptualization was carried out by J.W. and M.D.L. Data analysis was performed by J.W. and D.A.F. Synthetic modelling was carried out by J.W. J.W., M.D.L. and D.A.F. were responsible for methodology. Visualization was carried out by J.W. J.W. and M.D.L. wrote the paper.

Competing interests

The authors declare no competing interests.

Additional information

Extended data is available for this paper at https://doi.org/10.1038/s41561-024-01386-5.

Supplementary information The online version contains supplementary material available at https://doi.org/10.1038/s41561-024-01386-5.

Correspondence and requests for materials should be addressed to Jonathan Wolf.

Peer review information *Nature Geoscience* thanks Samantha Hansen, Barbara Romanowicz and Sebastian Rost for their contribution to the peer review of this work. Primary Handling Editors: Alireza Bahadori and James Super, in collaboration with the *Nature Geoscience* team.

Reprints and permissions information is available at www.nature.com/reprints.
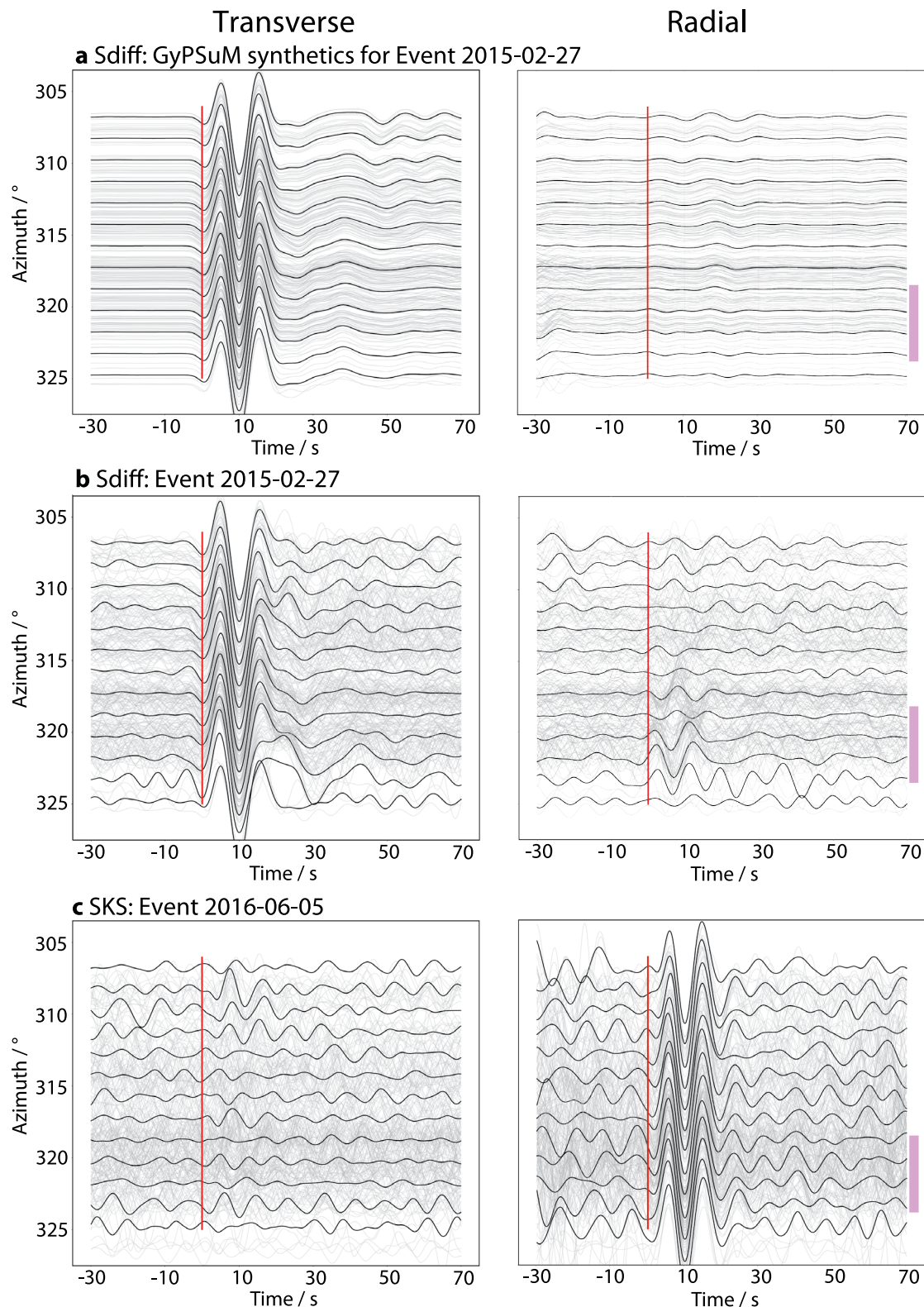
Extended Data Fig. 1 | Synthetic and real transverse component (left column) and radial component (right column) velocity seismograms for event 1. Seismograms are stacked linearly in 1.5° azimuth bins, after alignment to their maximum transverse amplitudes. Stacks are shown in black and individual seismograms in gray. Red lines indicate approximate arrival times. **a** AxiSEM3D synthetics using the 3D tomography model GyPSuM for Sdiff waveforms. Predicted radial amplitudes are very small, especially for large azimuths. Seismograms are normalized to maximum transverse amplitudes. **b** Real Sdiff waveforms with the same plotting conventions are in panel **a**. **c** Real SKS waveforms for a different event (2016-06-05) with a more favorable initial polarization for SKS analysis. Pink bars indicate the azimuths at which Sdiff is strongly split while SKS is not (compare panels **b** and **c**). Seismograms are normalized to maximum radial amplitudes.
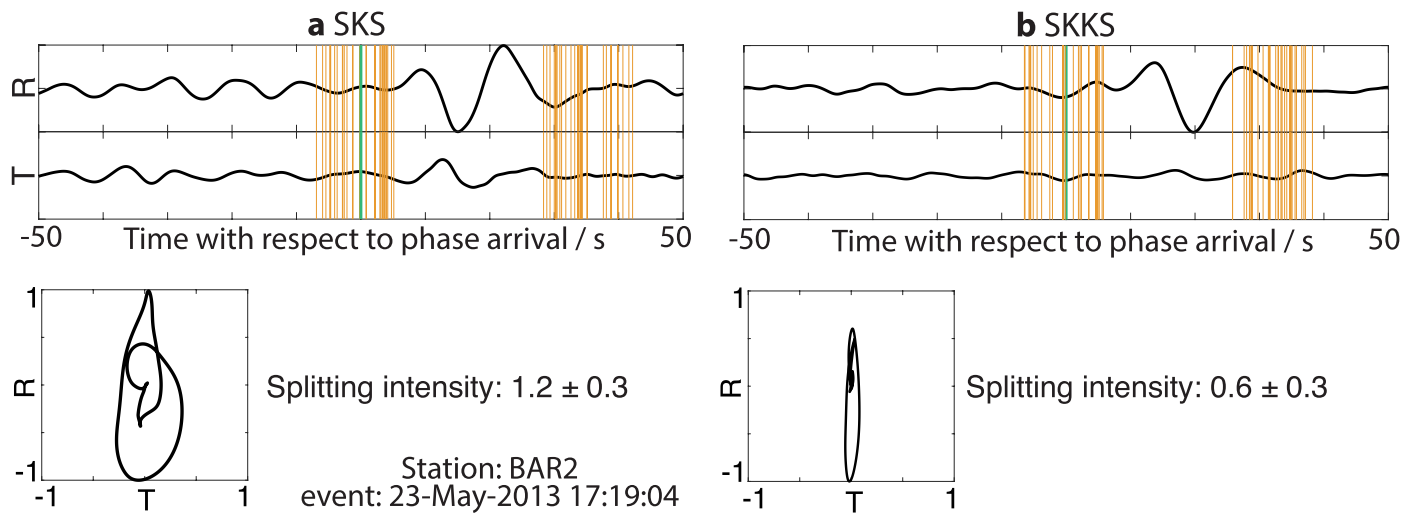
Extended Data Fig. 2 | Splitting diagnostic plots from SplitRacer that show an example of differential SKS-SKKS splitting recorded at seismic station BAR2 for an event that occurred on May 23, 2013. a SKS splitting; top panel: Radial (R) and transverse (T) component waveforms. The PREM-predicted SKS arrival time is shown as a green line, and the start/end of the 30 randomly chosen measurement time windows with orange lines. Bottom left: Elliptical SKS particle motion. **b** Same as panel **a** for the SKKS phase. The SKKS particle motion is closer to linear than for SKS. Therefore, SKS-SKKS splitting is discrepant.
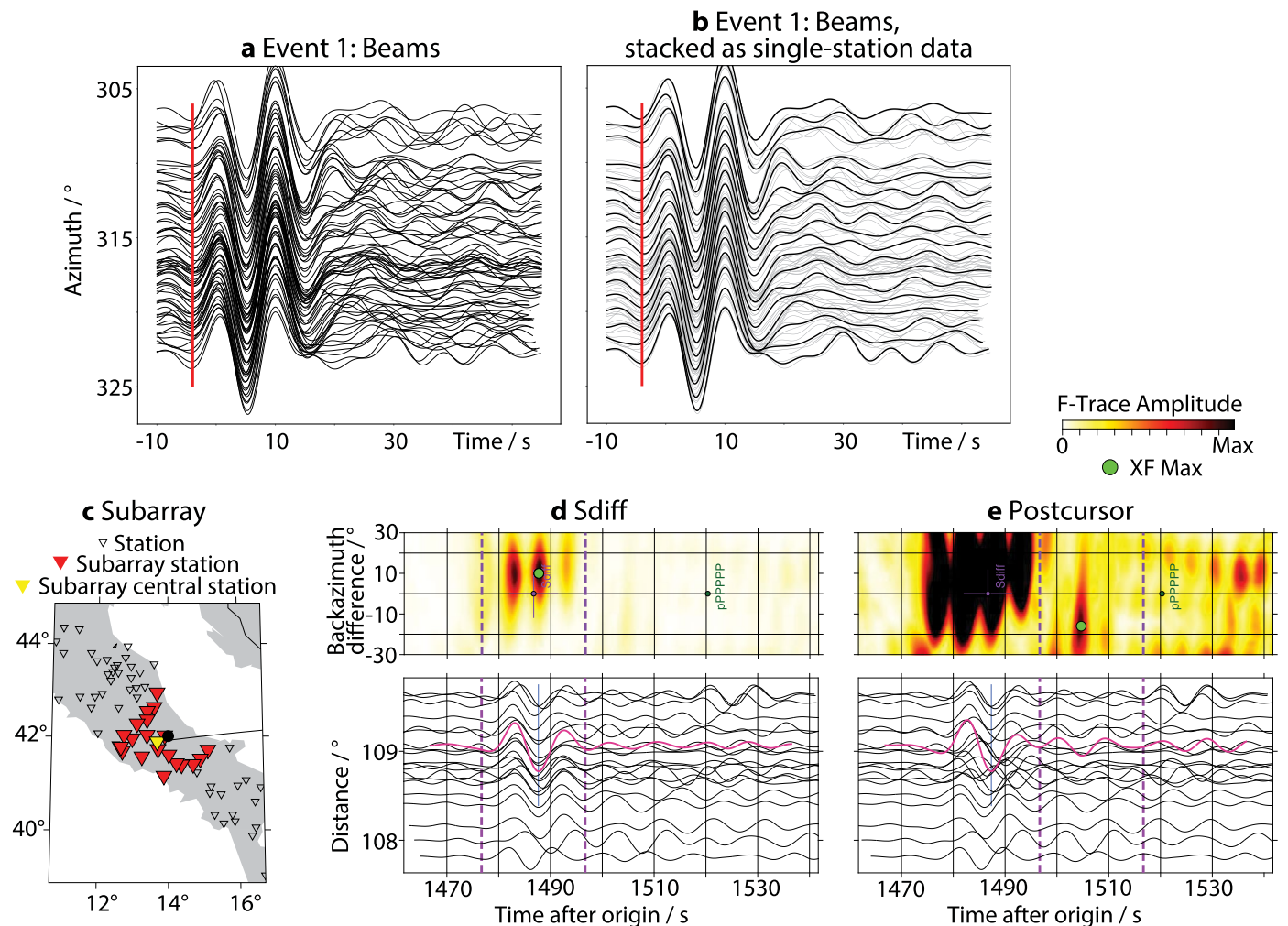
Extended Data Fig. 3 | Beamforming results. a Beamformed transverse velocity seismograms for event 1, showing the raw Sdiff beams as a function of azimuth. Beams are bandpass-filtered to retain periods between 7 and 20 and aligned with respect to the maximum Sdiff amplitudes. **b** As panel **a** but beams are stacked in the same way as single-station data, in 1.5° azimuthal intervals. Beams are shown in gray and stacks in black. In both panels, postcursors are visible. **c** Example subarray for which we conduct beamforming. Stations, shown as inverted triangles (see legend), are located in Italy. The backazimuth from which the Sdiff wave is predicted to arrive is shown at the central station as a black line. **d** Upper panel: F-Trace amplitude as a function of backazimuth and arrival time

(see legend). The maximum F-Trace value is shown as a green circle. The time window for which beamforming was performed is indicated by dashed violet lines. Lower panel: Single station seismograms are shown in as black lines and the beam as a pink solid line. **e** Plotting conventions are the same as in panel **d** but beamforming was performed for the postcursor, which arrives from a slightly different backazimuth than the main Sdiff arrival (panel **d**). To amplify the weak postcursor, the color scale in panel **e** is saturated by 10 times relative that in **d**. The postcursor arrives from a more northerly backazimuth than the main Sdiff phase, as expected for a ULVZ in our suggested location.